Article:
Bi, Yanding, Fu, Weinong, Niu, Shuangxia et al. (2 more authors) (2023) Torque Enhancement of a Dual-PM Flux Switching Machine with Improved Multiple High-Order Working Harmonics. IEEE Transactions on Transportation Electrification. ISSN: 2332-7782

https://doi.org/10.1109/TTE.2023.3294189

Torque Enhancement of a Dual-PM Flux-Switching Machine with Improved Multiple High-Order Working Harmonics

Yanding Bi[1], Weinong Fu[2], Shuangxia Niu[1], *Senior Member, IEEE*, Xing Zhao[3], *Member, IEEE*, Jiahui Huang[1], and Zhenyang Qiao[2]

[1]Department of Electrical Engineering, The Hong Kong Polytechnic University, Hong Kong, eesxniu@polyu.edu.hk
[2]Shenzhen Institutes of Advanced Technology, Chinese Academy of Sciences, Shenzhen, China, wn.fu@siat.ac.cn
[3]Department of Electronic Engineering, University of York, United Kingdom, xing.zhao@york.ac.uk

***Abstract*—In this paper, a novel E-core dual-permanent magnet flux-switching (DPM-FS) machine is proposed for traction applications in electrified transportation. The key is that an extra set of permanent magnet (PM) source is artfully inserted into stator slot openings, which has a parallel main flux path with spoke-type PMs, significantly improving the utilization ratio of the stator core as well as alleviating the magnetic saturation in the iron core. As a result, the proposed machine exhibits a bidirectional flux improvement ability of multiple working harmonics. The working harmonics of air-gap flux density with positive contributions to torque production are greatly enhanced, and those with negative influences are effectively suppressed. Compared with a conventional E-core FSPM machine with the same PM volume, the proposed machine exhibits a 42.8% higher open-circuit back electromotive force (EMF) and a 38.5% higher average output torque. A magnetomotive force (MMF)-permeance model is established to investigate the working principle of the proposed machine. Furthermore, the effectiveness of the proposed design is verified by using finite element analysis (FEA) and experimental results.**

***Index Terms*—Bidirectional flux improvement, finite element analysis, flux modulation principle, flux-switching machine, torque density.**

I. Introduction

PERMANENT magnet (PM) machines have attracted extensive attention due to the intrinsic advantages of high torque density and high efficiency [1], which have been widely applied in electrified transportation, especially in electric vehicles (EVs) and hybrid electric vehicles (HEVs) [2]. According to the location of PMs, PM machines can be classified into rotor PM machines [3], [4], stator PM machines [5], and dual PM machines [6]. Compared with other rotor-type electric machines, the stator PM machines have PMs and armature windings located on a stator and employ a simple salient-pole rotor, which possesses the merits of robust rotor structure and good heat dissipation ability [7].

The working principle of stator PM machines can be generally explained by a flux modulation principle [8]. However, the arrangements of PM on the stator have diversiform topologies according to the machine types. Nowadays, various types of stator PM machines have been reported in the literature, including flux-reversal PM (FRPM) machines [9]-[12], doubly salient PM (DSPM) machines [13], [14], and flux-switching PM (FSPM) machines [15]-[17]. Nonetheless, the torque density of FRPM machines and DSPM machines are inferior due to the defects of PM topologies that result in a small magnet volume or a low PM utilization ratio.

As one major category of stator PM machines, FSPM machines have the advantage of high torque density with the inherent flux concentration effect of the spoke-type PM topology [15]. A U-core FSPM machine was proposed at first in [17], which has 12 stator slots and fractional-slot concentrated winding (FSCW). Furthermore, outer-rotor structures have been adopted in U-core FSPM machines to improve torque performance [18]. However, the low PM utilization ratio significantly limits the torque density of U-core FSPM machines. In recent decades, various novel FSPM machine topologies have been proposed to improve machine performance, especially the torque density and torque ripple [19]-[21]. A multi-tooth FSPM machine was proposed in [19], which investigated the effect of employing auxiliary teeth on stator poles. The results show that utilizing four teeth on one stator pole can improve torque density significantly. A C-core FSPM machine was proposed in [20]. The usage of PM materials can be significantly reduced, and the slot area is largely increased. As a result, the C-core FSPM machine exhibits a 40% larger back electromotive force (EMF). A fault-tolerance FSPM machine with E-core stator segments was further proposed in [21]. In that design, extra teeth are inserted in stator slots, which separate the armature windings of different phases. Compared with conventional FSPM machines, the E-core FSPM machine has half PM usage, and an elevation of 15% torque density is achieved. In addition, novel FSPM machines with flux bridges have been proposed in [22-24] to solve the flux barrier effect of spoke-type PM configuration. The flux-focusing effect can be simultaneously enhanced due to the U-shaped PM array in [24]. However, the torque density of the aforementioned FSPM machines is far from sufficient to

be applied in the traction application of EVs. Furthermore, a double-stator FSPM machine [25] has been proposed to reduce the magnetic saturation of the stator, and a partitioned-rotor FSPM machine with a serial flux path [26] has been proposed to reduce the leakage flux and increase the PM utilization ratio. Nonetheless, two layers of air-gap result in complicated machine structures, and the manufacturing cost has significantly increased.

To further improve the torque performance of FSPM machines, recently, topologies with more than one set of PM sources have been investigated [27]-[30]. In [27], radially magnetized PMs were inserted into the stator tooth tip of FSPM machines. The extra PMs could significantly enhance the output torque without leading to stator magnetic saturation. A multi-tooth FSPM with an extra set of PMs between the auxiliary teeth was proposed in [28]. The proposed machine PM exhibited a 30.8% improvement in output torque, significantly enhancing the torque density. Nonetheless, the additional set of stator PMs in these machines only produces a small portion of total output torque, which results in limited improvement of torque density. Moreover, a novel FSPM machine with three sets of PMs was proposed in [29]. Rotor PMs and dummy slot PMs were innovatively added, which achieved a 200% torque density enhancement due to the addition of the two extra PM sets. A dual-sided FSPM machine with U-shaped stator PMs was proposed in [30]. The addition of consequent-pole rotor PMs resulted in a torque density increase of two times that of the stator U-shaped PM FS machine. However, the simplicity and robustness of the rotor structure are compromised in dual-sided PM FS machines. As a result, additional reinforcement of the rotor structure is required, which further increases the overall complexity of the machine. Meanwhile, the problems of low iron core utilization ratio and magnetic saturation still exist and hinder the application of FSPM machines.

In this paper, a novel E-core dual-PM flux-switching (DPM-FS) machine is proposed, which integrates a set of slot PMs into an E-core FSPM machine to improve the working harmonic distribution of the air-gap flux density. The magnetization directions of two sets of PMs are artfully designed to achieve a parallel flux path, which significantly improves the utilization ratio of the side teeth of stator E-core segments and alleviates the overall magnetic saturation in the iron core. As a result, the slot PMs can produce a significant portion of total output torque. In Section II, the topology of the proposed machine is first introduced. Subsequently, the working principle of the proposed machine is analyzed from the flux linkage distribution patterns. Section III emphasizes the bidirectional flux improvement principle by establishing a magnetomotive force (MMF)-permeance model. In addition, Section IV presents the global optimization of the proposed machine. Moreover, the electromagnetic performance of the conventional E-core FSPM machine and proposed DPM-FS machines is compared in Section V. The results show that the open-circuit flux linkage, back EMF, and torque density of the proposed machine are significantly improved. A prototype of the proposed machine is fabricated, and experiment results are presented in Section VI. Finally, a conclusion is drawn to summarize the main contributions of this study.

II. Machine Topology and Working Principle

A. Machine Topology

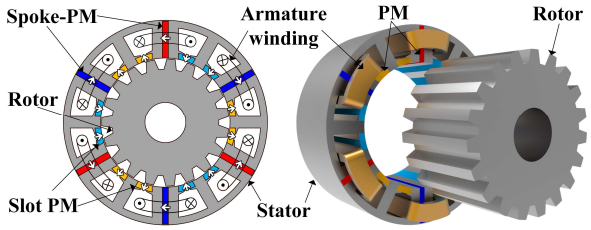

Fig. 1. Topologies of the proposed E-core DPM-FS machine.

As a type of flux modulation machine, FSPM machines utilize multiple harmonics of air-gap flux density to produce open-circuit back EMF and output torque. However, specific working harmonics can produce either positive or negative contributions to the total torque. Therefore, improving the harmonic distribution of the air-gap flux density is a viable approach to enhance the torque performance. According to this design guidance, the integration of an additional set of PMs can be leveraged to modify the MMF excited by the stator while considering the effect of stator slotting. An FRPM machine with slot PMs has been proposed in a previous study [11]. Compared to FRPM machines with surface-mounted PMs on stator teeth, this machine exhibits an increased torque density due to a significant reduction of flux leakage. Meanwhile, an E-core FS machine adopts a parallel-tooth design on the stator [21], which provides spaces for the integration of slot PMs. In this paper, by artfully combining the slot PM topology into the E-core FS machine, the DPM-FS machine is proposed.

The topology of the proposed E-core DPM-FS machine is shown in Fig. 1, including the 2D cross-sectional view and 3D view. Several E-core segments connected by thin flux bridges constitute the stator core. The spoke-type PMs are inserted between the side teeth of adjacent E-cores. Meanwhile, compared with the conventional E-core FS machine, the proposed machine has an extra set of PMs inserted in stator slot openings, which is magnetized in the radial direction. The slot PMs in the same E-core segment have identical magnetization directions, while the PMs in adjacent E-core segments have opposite directions. In addition, the rotor adopts a salient-pole topology, which provides high mechanical robustness. As shown in Fig. 1, a single-layer FSCW is used, which has short end-winding and enhances the fault-tolerance ability because of the isolation of windings in different phases.

B. Working Principle of E-core DPM-FS Machine

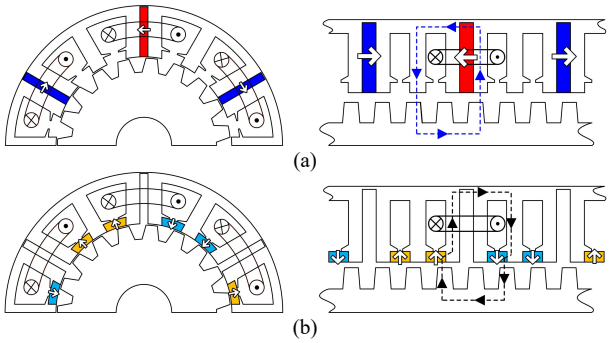

Fig. 2. Illustration of the stator PM sets and the corresponding flux circuits. (a) Spoke-type PM set. (b) Slot PM set.

In order to explicitly illustrate the working principle, the topologies of the proposed machine with a single set of spoke-type PMs and slot PMs are presented in Fig. 2 (a) and (b), respectively. As shown in Fig. 2, the flux excited by spoke-type PMs and slot PMs is represented by the dashed line in blue and the dashed line in black, respectively, which form a parallel magnetic circuit path by flowing through the side teeth at both sides of the spoke-type PM, middle teeth, and rotor.

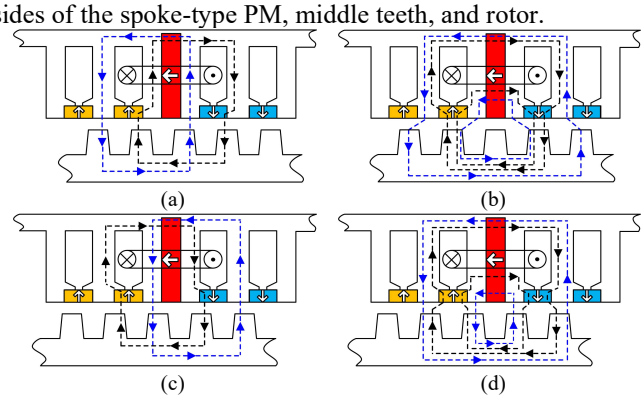

Fig. 3. Illustration of open-circuit PM excited flux at typical rotor positions (a) Position A. (b) Position B. (c) Position C. (d) Position D.

Furthermore, Fig. 3 shows the magnetic flux circuit of dual-PM at four typical rotor positions, which reveals the superposition principle of flux linkage. The flux distribution at the typical rotor positions corresponds to the position A to D in the phase flux linkage waveform, as shown in Fig. 4. Fig. 3 (a) and (c) show the negative and positive extreme positions of the flux linkage, where a rotor tooth is aligned with an E-core side tooth. At these positions, the magnetic flux excited by the dual sets of PMs passes through the armature coils in an identical direction, and maximum or minimum values of the phase flux linkage can be achieved. Consequently, the utilization of the stator core is significantly improved due to the parallel magnetic circuit. In contrast, as shown in Fig. 3 (b) and (d), when the rotor rotates to the positions where the rotor teeth are unaligned or evenly aligned with the stator side teeth, the flux forms a complete circuit without crossing the phase coils, resulting in zero flux linkage. Moreover, the spoke-type PM and slot PM excited flux have opposite directions in the E-core middle teeth, stator yoke, and rotor, greatly relieving the magnetic saturation on the stator and rotor cores.

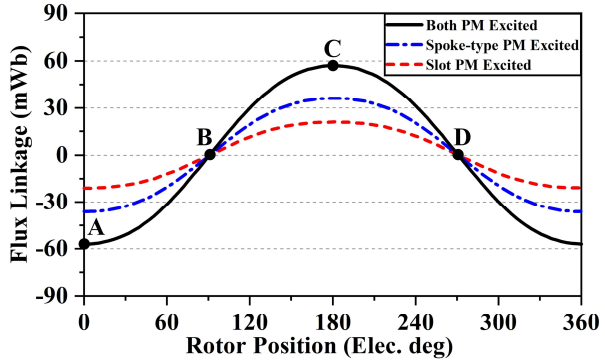

Fig. 4. Open-circuit flux linkage of the proposed machine.

In order to verify the analysis mentioned above, a finite element analysis (FEA) result of open-circuit phase flux linkage is obtained. Fig. 4 exhibits a bipolar phase flux linkage with dual sets and single-set PM excitations. The spoke-type and slot PM excited flux linkages have no phase difference. As a result, the phase flux linkage with both PM excitations is the superposition of two single PM sets, which reveals the torque enhancement mechanism of the proposed design.

III. Quantitative Analysis of Bidirectional Flux Improvement of Multiple Working Harmonics

FSPM machines can be classified as one type of flux-modulation machine [7]. Thus, the torque generation principle of the proposed E-core DPM-FS machine can be explained by the flux modulation effect. In this section, an MMF-permeance model is established to quantitatively investigate the contribution of multiple working harmonics. The initial design parameters of the proposed DPM-FS machine and conventional E-core FS machine are listed in Table I. Meanwhile, the following assumptions are made in advance:

1) The permeance of stator and rotor iron cores is infinite, and the saturation effect in iron cores is neglected.
2) The positive rotational direction is set to be counterclockwise.
3) The original position is set as the minimum of stator MMF and the maximum of rotor permeance.

TABLE I
Initial Design Parameters of the Conventional and Proposed Machines

Parameters	Unit	Conventional machine	Proposed machine
Stator outer diameter	mm	120	
Active stack length	mm	50	
Air-gap length	mm	0.6	
Rotor pole number	-	19	
Stator inner diameter	mm	76	
Stator yoke thickness	mm	4	
Magnetic bridge thickness	mm	1	
E-core side tooth thickness	mm	6	
E-core middle tooth thickness	mm	7	
Spoke-type PM thickness	mm	3.5	
Slot PM thickness	mm	-	3.5
Rotor tooth thickness	mm	6	
Rotor tooth outer width ratio	-	0.4	
Rotor tooth inner width ratio	-	0.7	

A. Analysis of Air Gap Flux Density

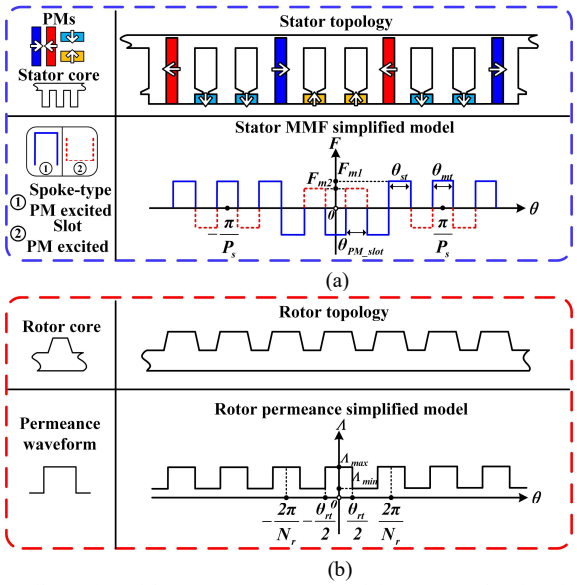

Fig. 5. Illustration of the MMF-permeance model. (a) Stator sketch and ideal MMF function. (b) Rotor sketch and ideal permeance function.

Fig. 5 illustrates the simplified-stator MMF and rotor permeance equivalent functions. As shown in Fig. 5 (a), the spoke-type PM excited MMF is depicted by the solid line in blue, and the dashed line in red depicts the slot PM excited MMF. Compared with the spoke-type PMs, the slot PM excited MMF has an opposite direction in stator slot positions. F and θ denote the MMF and the circumferential angle in the air-gap, respectively. θ_{st}, θ_{mt}, and θ_{PM_slot} are the angular spans of the side tooth, middle tooth, and slot PM, respectively. F_{m1} and F_{m2} are the amplitudes of spoke-type and slot PMs excited MMF, respectively. In addition, P_s is the pole-pair number of the fundamental order of equivalent stator MMF, which is given as

$$P_s = \frac{N_s}{4} \tag{1}$$

where N_s is the number of stator slots.

The air-gap permeance function considering both stator and rotor slotting effects is given as [15]

$$\Lambda(\theta,t) = \frac{g}{\mu_0}\Lambda_s(\theta)\Lambda_r(\theta,t) \tag{2}$$

where g is the length of air-gap, μ_0 is the permeability of air. Meanwhile, permeance functions $\Lambda_s(\theta)$ and $\Lambda_r(\theta,t)$ are utilized to model the stator and rotor slotting effects, respectively.

Subsequently, the air-gap flux density can be derived as

$$B_g(\theta,t) = F_{PM}(\theta)\Lambda(\theta,t) = \frac{g}{\mu_0}F_{PM}(\theta)\Lambda_s(\theta)\Lambda_r(\theta,t) \tag{3}$$

where $F_{PM}(\theta)$ is the PM-excited MMF function. Here, an equivalent stator MMF function is defined by considering the stator slotting effect on PM-excited MMF, which is given as

$$F_{eq}(\theta) = \frac{g}{\mu_0}F_{PM}(\theta)\Lambda_s(\theta) = \sum_{i=1,3,5...}^{\infty} F_{eqi}\cos(iP_s\theta) \tag{4}$$

where F_{eqi} is the amplitude of the ith-order harmonic of the equivalent stator MMF.

Fig. 6 (a) shows the air-gap flux density excited by the single and dual sets of PMs. The spoke-type and slot PMs excited air-gap flux densities exhibit good consistency with the equivalent model of stator MMF. In the meantime, the air-gap flux density excited by dual sets of PMs is the superposition of two single sets of PMs. As shown in Fig. 6 (b), the slot PMs decrease the 1st- and 3rd-order harmonics and enhance the 5th-, 15th-, and 17th-order harmonics. More specifically, the harmonics with positive contributions to open-circuit phase back EMF are improved, and those with negative contributions are reduced.

In the meantime, Fig. 5 (b) depicts the topology of the salient-pole rotor and the equivalent function of rotor permeance. Λ denotes permeance. Λ_{max} *and* Λ_{min} represent the maximum and minimum values of rotor permeance, respectively. θ_{rt} is the angular span of the rotor tooth, and N_r is the number of rotor poles. Due to the slotting effect, the distribution of rotor permeance is not uniform, which can be derived as

$$\Lambda_r(\theta,t) = \Lambda_{r0} + \sum_{j=1,2,3...}^{\infty}\Lambda_{rj}\cos(jN_r(\theta-\omega_r t)) \tag{5}$$

where Λ_{r0} is the average value, and Λ_{rj} is the amplitude of the jth-order harmonic of the rotor permeance. Additionally, ω_r is the mechanical angular speed of the rotor.

Furthermore, the overall air-gap flux density can be derived by combining (3) - (5), which is shown as follows.

$$\begin{aligned} B_g(\theta,t) &= F_{eq}(\theta)\Lambda_r(\theta,t) \\ &= \sum_{i=1,3,5...}^{\infty} F_{eqi}\Lambda_{r0}\cos(iP_s\theta) \\ &+ \sum_{i=1.3.5...}^{\infty}\sum_{j=1,2,3...}^{\infty}\frac{F_{eqi}\Lambda_{rj}}{2}\cos[(iP_s+jN_r)(\theta-\frac{jN_r}{iP_s+jN_r}\omega_r t)] \\ &+ \sum_{i=1.3.5...}^{\infty}\sum_{j=1,2,3...}^{\infty}\frac{F_{eqi}\Lambda_{rj}}{2}\cos[(iP_s-jN_r)(\theta+\frac{jN_r}{iP_s-jN_r}\omega_r t)] \end{aligned} \tag{6}$$

The pole-pair numbers and electrical angular speed of the harmonics of air-gap flux density are shown in Table II. Based on the distribution function of stator PM MMF, the harmonic order i can only be odd numbers. Consequently, the orders of i up to 19 are considered since the amplitudes of higher orders are negligible. The harmonic order j of the rotor permeance is selected to be one since the amplitudes of modulated air-gap flux density harmonics with higher orders of j are negligible.

TABLE II
POLE PAIRS AND ROTATION SPEED OF AIR-GAP FLUX DENSITY HARMONICS

Pole pairs	Rotation speed
iP_s+jN_r	$jN_r\ \omega_r/(iP_s+jN_r)$
$\lvert iP_s-jN_r\rvert$	$jN_r\ \omega_r/(\lvert iP_s-jN_r\rvert)$

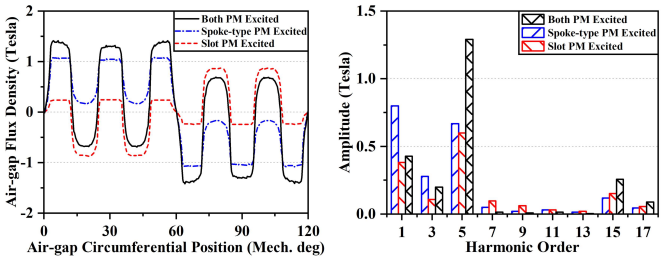

Fig. 6. Open-circuit air-gap flux density of different PM excitations of the proposed machine. (a) Waveforms. (b) Harmonic distributions.

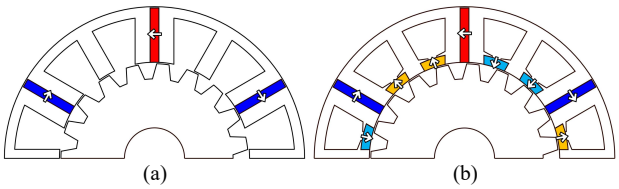

Fig. 7. Topologies of the conventional and proposed machines. (a) Conventional E-core FS machine. (b) Proposed DPM-FS machine.

Fig. 7 illustrates the topologies of the conventional E-core FS machine and the proposed DPM-FS machine. In order to explicitly demonstrate the merits of the DPM design, both machines are investigated regarding the air-gap flux density and open-circuit phase back EMF. The air-gap flux density considering the rotor slotting effect is shown in Fig. 8. Fig. 8 (a) exhibits the waveforms of the conventional and proposed machines. Meanwhile, the harmonic distributions of both machines are shown in Fig. 8 (b), and the main working harmonics are marked in the plot. The proposed E-core DPM-FS machine has multiple working harmonics, among which the amplitudes of 2, 4, and 8 pole pairs are significantly larger than the conventional machine, and the amplitudes of 16, 22, and 28 pole pairs are smaller than the conventional machine.

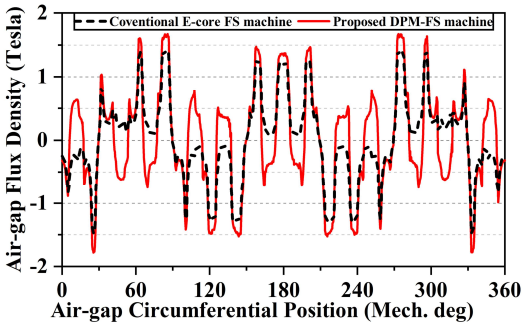

(a)

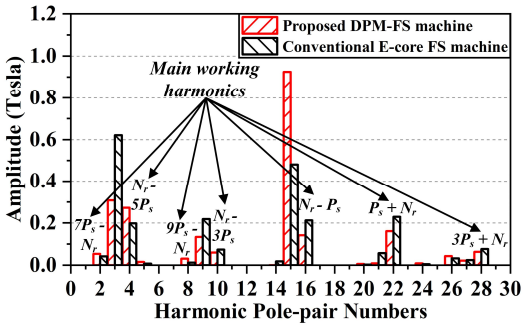

(b)

Fig. 8. Air-gap flux density of the conventional and proposed machines. (a) Waveforms. (b) Harmonic distributions.

B. Analysis of Harmonic Contributions to the Production of Open-circuit Phase Back EMF and Output Torque

Multi-working harmonics of air-gap flux density in the conventional and proposed machines contribute to the production of phase back EMF and output torque. In order to analyze the contribution of specific harmonics, the phase back EMF is quantitively analyzed, which is derived as follows.

$$E_{ph}(t) = -\frac{d}{dt}[r_g l_{st} \int_0^{2\pi} B_g(\theta,t) N_w(\theta) d\theta] \tag{7}$$

where r_g is the inner radius of the stator, l_{st} is the active stack length, and $N_w(\theta)$ is the winding function, which is given as [11]

$$N_w(\theta) = \sum_{v=1,3,5...}^{\infty} \frac{2}{\pi v} \frac{N_c}{P_a} k_{wv} \cos(vP_a\theta) \tag{8}$$

where N_c is the winding turns per phase. v and k_{wv} are the order number and the winding factor of the harmonics of armature winding, respectively. Additionally, P_a is the fundamental pole-pair number of armature winding.

Then, the contribution of multi-working harmonics to the generation of open-circuit phase back EMF is investigated. As shown in Fig. 8 (b), the pole-pair numbers of the main working harmonics are even. As a result, (6) can be further expressed as

$$\begin{aligned} E_{ph}(t) &= -\frac{d}{dt}[r_g l_{st} \int_0^{2\pi} B_g(\theta,t) N_w(\theta) d\theta] \\ &= 2 r_g l_{st} N_c N_r \omega_r \sin(N_r\omega_r t) \sum_n^{\infty} \frac{B_{gn} k_{wn}}{n} \\ &= 2 r_g l_{st} N_c N_r \omega_r \sin(N_r\omega_r t)[\frac{B_{g2}k_{w2}}{7P_s - N_r} + \frac{B_{g4}k_{w4}}{N_r - 5P_s} \\ &+ \frac{B_{g8}k_{w8}}{9P_s - N_r} + \frac{B_{g10}k_{w10}}{N_r - 3P_s} - \frac{B_{g14}k_{w14}}{11P_s - N_r} - \frac{B_{g16}k_{w16}}{N_r - P_s} \\ &- \frac{B_{g22}k_{w22}}{P_s + N_r} + \frac{B_{g26}k_{w26}}{15P_s - N_r} + \frac{B_{g28}k_{w28}}{3P_s + N_r} + \frac{B_{g34}k_{w34}}{5P_s + N_r}] \end{aligned} \tag{9}$$

where n, B_{gn}, and k_{wn} are the pole-pair numbers, the amplitude of air-gap flux density, and the winding factor of working harmonics, respectively.

The contribution of specific harmonics is shown in Table III. The amplitudes of air-gap flux density harmonics are obtained from the FEA results, and the harmonic contribution is calculated using (9). On the one hand, with the addition of slot PMs, the harmonics with positive contributions to phase back EMF are enhanced, including the 2, 4, 8, and 34 pole pairs harmonics. The total back EMF is vastly increased due to the increase of these harmonics. On the other hand, the harmonics of 14, 16, and 22 pole pairs reduce the total phase back EMF due to the negative winding factors. However, the slot PMs significantly decrease the amplitudes of these harmonics, lessening negative back EMF production. Consequently, the total back EMF increased by 58%. Moreover, the analytical results of total phase back EMF are compared with FEA results, which exhibit a high accuracy with errors of less than 5%.

TABLE III
OPEN-CIRCUIT BACK EMF AND TORQUE CONTRIBUTIONS OF MULTIPLE WORKING HARMONICS IN CONVENTIONAL AND PROPOSED MACHINES

Pole pairs	k_{wv}	Conv. E-core FS machine	Prop. DPM-FS machine
		B_g (T)/E_{ph} (V)/ T_{avg} (Nm)	B_g (T)/E_{ph} (V)/ T_{avg} (Nm)
$7P_s$ - N_r, 2	0.5	0.04/16.4/0.99	0.05/21.2/1.29
N_r - $5P_s$, 4	0.866	0.19/68.1/4.14	0.27/93.3/5.67
$9P_s$ - N_r, 8	0.866	0.01/2.0/0.12	0.03/5.3/0.32
$5P_s$ + N_r, 34	0.5	0.2/4.7/0.29	0.3/7.0/0.42
N_r - $3P_s$, 10	0.5	0.07/5.8/0.35	0.06/4.8/0.29
$15P_s$ - N_r, 26	0.5	0.03/1.0/0.06	0.04/1.3/0.08
$3P_s$ + N_r, 28	0.866	0.08/3.8/0.23	0.06/3.1/0.19
$11P_s$ - N_r, 14	-0.5	0.018/-1.0/-0.06	0.0005/-0.03/-0.002
N_r - P_s, 16	-0.866	0.21/-18.2/-1.11	0.14/-12.2/-0.74
P_s + N_r, 22	-0.5	0.23/-8.3/-0.5	0.16/-5.8/-0.35
Total E_{ph}–analytical (V)		74.3	117.9
Total E_{ph}–FEA (V)		77.5	116.1
Total T_{avg}–analytical (Nm)		4.51	7.17
Total T_{avg}–FEA (Nm)		4.38	7.05

Moreover, when the reluctance torque is ignored, the total average torque can be calculated as

$$T_{avg} = \frac{3}{2}\frac{I_m E_{ph}}{\omega_r} = 3 I_m r_g l_{st} N_c N_r \sum_n^{\infty} \frac{B_{gn} k_{wn}}{n} = \sum_n^{\infty} T_{avgn} \tag{10}$$

where I_m is the peak value of phase current, and T_{avgn} is the torque component produced by the n pole-pair harmonics.

In order to demonstrate the enhanced torque generation ability of the proposed DPM-FS machine, a phase current of 3A is injected into both the conventional and proposed machines. The torque contributions of multiple working harmonics are subsequently analyzed, and the results are presented in Table III. It can be seen that specific working harmonics produce positive torque, while others result in negative torque production. The integration of slot PMs modifies the distribution of the stator MMF, leading to improved working harmonics of 2, 4, 8, and 34 pole pairs through the modulation effect of the salient-pole rotor. As a result, the positive torque production of the proposed DPM-FS machine is substantially enhanced, which is consistent with the improvement of back EMF. Additionally, the magnitudes of 14, 16, and 22 pole-pair working harmonics are reduced, effectively suppressing negative torque generation. The analytical results demonstrate

high accuracy when compared to the FEA-predicted average torques in both the conventional E-core FS machine and the proposed DPM-FS machine, thus validating the effectiveness of the MMF-permeance model.

Therefore, by using the flux modulation principle, the bidirectional flux improvement effect is revealed. The working harmonics with positive contributions are enhanced, while those with negative contributions are weakened. Consequently, the proposed E-core DPM-FS machine possesses the advantage of enhanced phase back EMF and torque performance.

IV. Global Optimization of the Proposed Machine

In this section, the global optimization of the proposed E-core DPM-FS machine is presented. The main structural design parameters of the proposed machine are illustrated in Fig. 9. During the optimization process, the stator outer diameter, air-gap length, active stack length, PM volume, and copper loss remain constant.

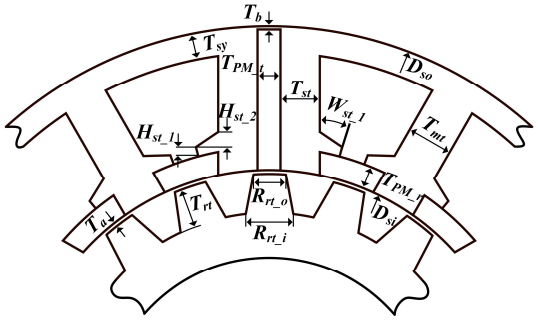

Fig. 9 Structural design parameter illustration of the proposed machine.

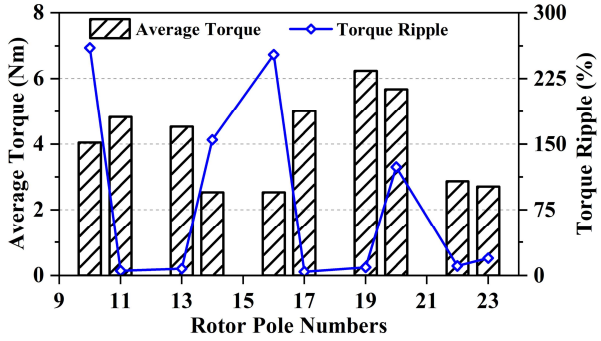

Fig. 10. Average torque and torque ripple of the proposed machine with different rotor pole numbers.

Before performing the global optimization, the influence of rotor pole numbers on machine performance is investigated. As shown in Fig. 3, the number of rotor teeth should be close to the total number of stator E-core side and middle teeth, which is 18. To perform a comprehensive analysis, the rotor pole numbers from 10 to 24 are considered except for integer multiples of 3. The results in Fig. 10 exhibit that when the rotor pole number is even, the torque ripple is too large to be accepted due to the high cogging torque. In contrast, the torque ripple is low with odd-number rotor poles. When the rotor has 19 poles, the maximum average torque and a torque ripple lower than 10% can be achieved, which is selected for further study.

The non-dominated sorting genetic algorithm II (NSGA-II) is utilized for the global optimization of the proposed machine [31]. The optimization ranges of the 13 variables are listed in Table IV. Due to a large number of optimization variables, the number of populations and generations is selected as 80 and 100, respectively. Meanwhile, the crossover and mutator factors are 0.9 and 0.1, respectively. Moreover, the objective functions and key design constraints are given as

$$min\begin{cases} f_1(x), & f_1(x)= -T_{avg} \\ f_2(x), & f_2(x)= T_{ripple} \end{cases} \tag{11}$$

$$\begin{cases} V_{PM}=36\ mL \\ P_{copper}=15.5\ W \\ T_{avg} \geq 3\ Nm \\ T_{ripple} \leq 15\% \end{cases} \tag{12}$$

where T_{avg} and T_{ripple} refer to average torque and torque ripple, respectively. Additionally, V_{PM} is the total volume of PMs, and P_{copper} refers to copper loss.

Fig. 11 shows the optimization results of the proposed machine. As shown in the plot, the Pareto front is clear, which validates the convergence of the global optimization. When the torque ripple is less than 5%, the machine with the highest torque is selected as the optimal design, which is marked by a yellow star.

TABLE IV
Optimization Range of Structural Design Parameters

Parameters	Unit	Range
Split ratio, D_{si}/D_{so}	mm	0.5~0.8
Stator yoke thickness, T_{sy}	mm	4~8
Stator magnetic bridge thickness, T_b	mm	1~3
E-core side tooth thickness, T_{st}	mm	3.5~8
E-core middle tooth thickness, T_{mt}	mm	3.5~8
Spoke-type PM thickness, T_{PM_t}	mm	3~7
Slot PM thickness, T_{PM_r}	mm	2.5~5
Stator tooth tip thickness, H_{st_1}	mm	0.8~2
Stator tooth skew thickness, H_{st_2}	mm	1~2
Stator tooth tip width, W_{st_1}	degree	4~7
Rotor tooth thickness, T_{rt}	mm	4~10
Rotor tooth outer width ratio, R_{rt_o}	-	0.2~0.7
Rotor tooth inner width ratio, R_{rt_i}	-	0.2~0.9

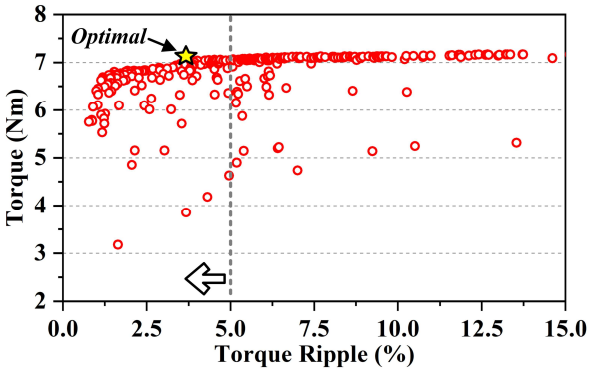

Fig. 11. Optimization results of the proposed E-core DPM-FS machine.

V. Comparative Study of Different FS Machines

In this section, the electromagnetic performances of the conventional E-core FS machine and proposed DPM-FS machine are compared. The open-circuit and on-load performance are investigated. Both machines are globally optimized with the same constraints for a fair comparison. The operating conditions and optimized design parameters are listed in Table V and Table VI, respectively.

A. Comparison of Open-circuit Performance

Fig. 12 (a) and (b) show the flux distribution of the conventional and proposed machines, respectively. In Fig. 12 (b), the spoke-type and slot PM excited flux are separately illustrated. The solid line in black is the main flux path, while the dashed line in red is the leakage flux path. The main flux distributions have a good consistency with the analysis shown in Fig. 3. Meanwhile, the two PM sets have an opposite direction of leakage flux distributions on the stator middle tooth, stator yoke, and rotor, which reduces the overall core saturation. As shown in Fig. 13 (b), the stator and rotor core of the proposed machine with dual sets of PMs has a significantly lower magnetic flux density than the conventional machine with only spoke-type PM excitation, as shown in Fig. 13 (a). As a result, the potential magnetic saturation with armature current can be avoided. However, local saturation occurs on the stator tooth tip due to the addition of slot PMs, which slightly influences the overload capacity of the proposed machine.

TABLE V
DETAILS OF MACHINE OPERATION PARAMETERS

Parameters	Unit	Values
Rated rotation speed	r/min	1000
Speed in direct-drive mode	r/min	300
Conductor turns per coil	-	105
PM material	-	N35UH
PM volume	mL	36
PM residual remanence	T	1.21
Steel material	-	B35A360
Copper loss under light load	W	15.5
Copper loss under normal load	W	80.0
Rated output power	W	1400
Cooling method	-	Natural cooling

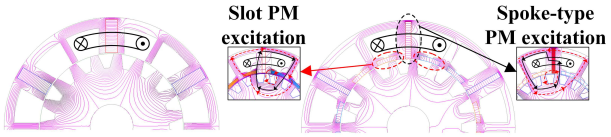

(a) (b)

Fig. 12. Open-circuit flux distribution. (a) Conventional E-core FS machine. (b) Proposed DPM-FS machine.

TABLE VI
OPTIMIZED DESIGN PARAMETERS OF THE MACHINES

Parameters	Unit	Conventional machine	Proposed machine
Stator outer diameter	mm	120	
Active stack length	mm	50	
Air-gap length	mm	0.6	
Rotor pole number	-	19	
Stator inner diameter	mm	78	76.6
Stator yoke thickness	mm	4.58	4.09
Magnetic bridge thickness	mm	1	1
E-core side tooth thickness	mm	3.88	4.96
E-core middle tooth thickness	mm	3.68	5.09
Spoke-type PM thickness	mm	6	3
Slot PM thickness	mm	-	2.5
Stator tooth tip thickness	mm	-	0.8
Stator tooth skew thickness	mm	-	1
Stator tooth tip width	degree	-	6.7
Rotor tooth thickness	mm	6.53	7.71
Rotor tooth outer width ratio	-	0.33	0.33
Rotor tooth inner width ratio	-	0.69	0.59

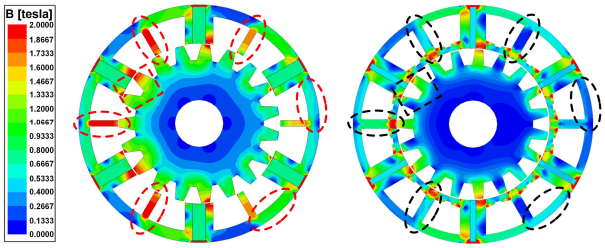

(a) (b)

Fig. 13. Open-circuit flux density distribution. (a) The optimized conventional machine. (b) The optimized proposed machine.

The comparison of phase flux linkage is shown in Fig. 14. Fig. 14 (a) shows that the bipolar flux linkage of the proposed machine is significantly improved due to the addition of slot PMs. The amplitude of the fundamental harmonic is shown in Fig. 14 (b). Compared with the conventional machine, the flux linkage of the proposed machine has a 42.9% increase.

To demonstrate the merits of the proposed machine, the phase back EMFs produced by the PM excitations with single and dual sets are investigated. Fig. 15 (a) shows that both the spoke-type and slot PM excited phase back EMFs have low high-order harmonic components. The spoke-type PM makes the major contribution to the total back EMF, while the slot PM also provides a considerable portion. As shown in Fig. 15 (b), the total phase back EMF is the superposition of the two single PM excitations, and the contribution of slot PMs is over 35%.

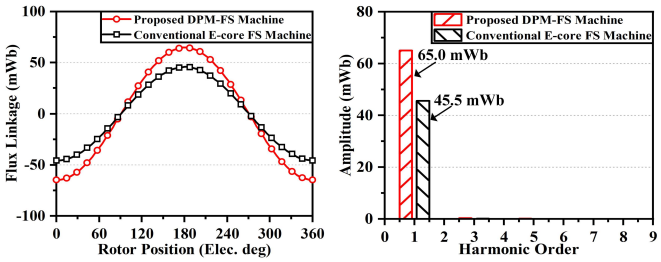

(a) (b)

Fig. 14. Open-circuit flux linkage of phase A of the conventional and proposed machines. (a) Waveforms. (b) Harmonic distributions.

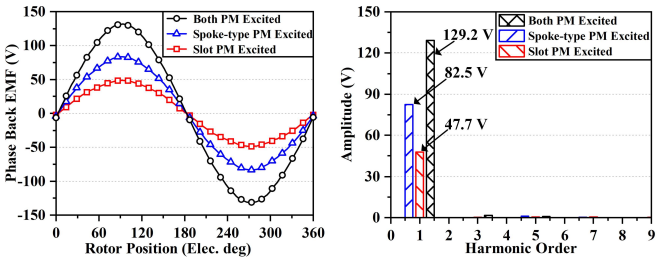

(a) (b)

Fig. 15. Open-circuit back EMF of phase A of the proposed machines with different PM excitations. (a) Waveforms. (b) Harmonic distributions.

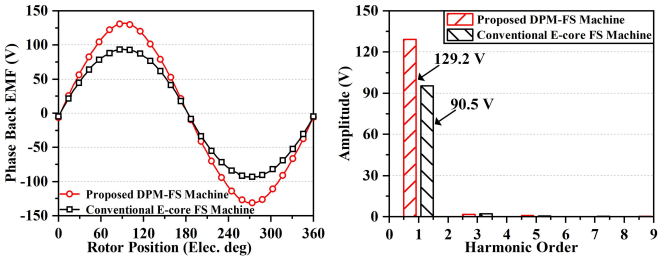

(a) (b)

Fig. 16. Open-circuit back EMF of phase A of the conventional and proposed machines. (a) Waveforms. (b) Harmonic distributions.

The comparison of phase back-EMFs is shown in Fig. 16. Compared with the conventional machine, the back-EMF of the proposed machine has a 42.8% enhancement at the rated rotational speed due to the addition of slot PMs, which shows a great consistency with the elevation of flux linkage.

B. Comparison of On-load Torque Performance

The on-load performance of the conventional and proposed machines is investigated in this part. The light load condition with a constant copper loss of 15.5 W is investigated, and a zero *d*-axis current (I_d=0) control strategy is utilized.

Fig. 17 (a) shows the plot of torque versus the current advancing angle. It demonstrates that both machines exhibit the maximum torque when the current advancing angle equals zero, which validates the selection of the I_d=0 control strategy. The torque versus different amplitudes of armature current is shown in Fig. 17 (b). When the current increases, the average torque of both machines elevates. The curve linearity of the proposed machine is improved compared with the conventional machine due to the magnetic saturation relieving effect. As a result, the proposed machine exhibits a better overloading ability.

Fig. 18 (a) shows the torque of the proposed machine. The spoke-type PMs contribute the main output torque, while the slot PMs provide 35.9% of the total torque. It is worth mentioning that the total torque with dual sets of PMs is larger than the summation of the torques of the two single sets of PMs. The reason lies in the alleviation of the magnetic saturation of stator and rotor cores, as shown in Fig. 13. The comparison of the output torques is shown in Fig. 18 (b). The proposed machine exhibits a 38.46% larger average torque, and the torque ripple is reduced from 4.14% to 3.53%.

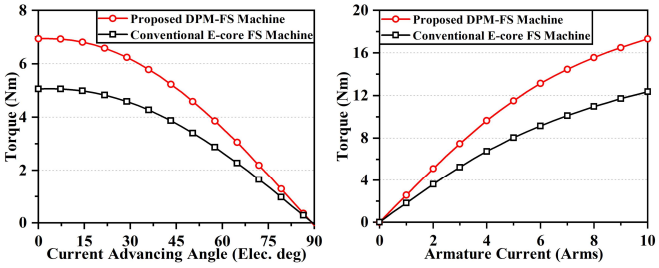

Fig. 17. Torque characteristics of the conventional and proposed machines. (a) Torque vs. current advancing angle. (b) Torque vs. armature current.

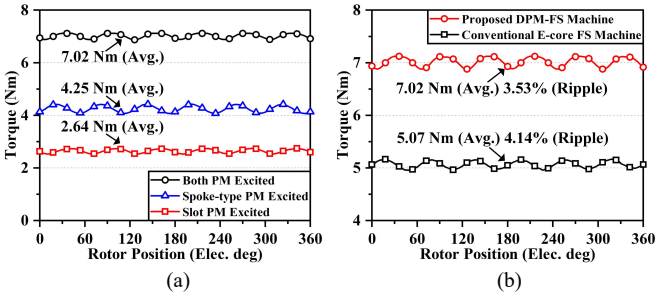

Fig. 18. Average torque at rated current. (a) The proposed machine with different excitations. (b) Comparison of average torques.

C. Performance Comparison at Different Operating Conditions

In this part, the performance of the conventional and proposed machines is comprehensively investigated and compared in different operating scenarios, including different operating speeds and load conditions.

Fig. 19 (a) shows the open-circuit back EMF waveforms of the conventional E-core FS machine and the proposed DPM-FS machine at 300 r/min and 1000 r/min. At both operating speeds, the proposed machine exhibits a significant improvement in the magnitudes of back EMFs. In the low-speed operating mode, the back EMF is increased from 27.13 V to 38.88 V. Meanwhile, the value is enhanced from 90.52 V to 129.2 V when the rotational speed is 1000 r/min. Moreover, the conventional and proposed machines exhibit sinusoidal waves with negligible high-order harmonics. The variation of open-circuit back EMFs at different operating speeds is depicted in Fig. 19 (b). Good linearity of back EMF magnitudes with increased speeds can be observed in both machines, and the improvement of back EMF in the proposed machine is demonstrated.

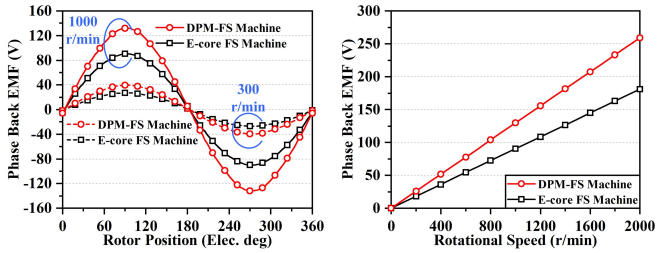

Fig. 19. Open-circuit back EMF of the conventional and proposed machines. (a) Waveforms at 300 r/min and 1000 r/min. (b) The magnitude of fundamental harmonic vs. rotational speed.

Fig. 20 shows the output torque under light and normal load conditions. In both operating conditions, the torque performance of the proposed DPM-FS is greatly enhanced compared to the conventional E-core FS machine. Under the light load condition, the average torque of the proposed machine is improved by 38.46%, as mentioned in the previous part. While under the normal load condition, a higher torque improvement of 41.68% is achieved, demonstrating the merit of the proposed DPM-FS machine in torque generation performance. In the meantime, the torque ripples of the proposed machine at both light load and normal load conditions are kept lower than 4%, as listed in Table VII. In contrast, the conventional machine exhibits an increased torque ripple of 5.85% under the normal load condition.

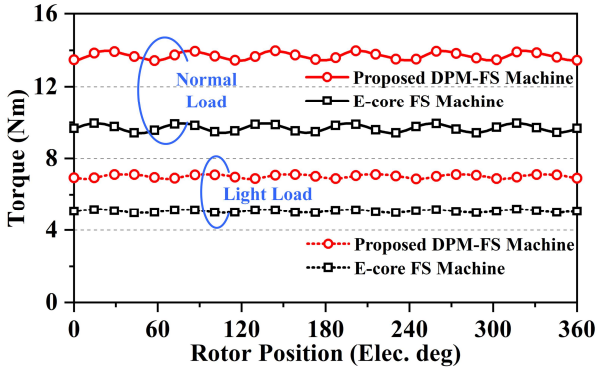

Fig. 20. Torque characteristics of the conventional and proposed machines under light and normal load conditions.

The losses and efficiencies of the proposed and conventional machines are investigated. As listed in Table VII, the iron loss, PM eddy-current loss, and copper loss are calculated. Due to the greatly improved average torque, the proposed machine

achieves increased power efficiency compared to the conventional machine at a rated speed of 1000 r/min, albeit the iron losses are higher due to local saturation. Furthermore, the efficiency maps of the conventional and proposed machines are calculated, as shown in Fig. 21 (a) and (b), respectively. The proposed machine demonstrates a higher maximum efficiency of 93.2%. Meanwhile, the high-efficiency region (where the efficiency is larger than 90%) is greatly widened to the region with larger torque values when the speed is lower than 1500 r/min. More specifically, except for the operating conditions with low torque values, the efficiency of the proposed machine can achieve an elevation of 1%~2% at the same speed and torque compared to the conventional machine, which demonstrates a much better energy conversion capability. Moreover, the torque of the proposed machine in the low-speed constant-torque region is greatly larger than the conventional machine, exhibiting an improved output power capability in low-speed operations. The power factors have been listed in Table VII under light load and normal load conditions. The proposed machine exhibits a much higher open-circuit back EMF compared to the conventional machine. However, the synchronous inductance also greatly increased due to the integration of slot PMs. Thus, a slight increase in the power factor of the proposed machine can be observed.

TABLE VII
ON-LOAD PERFORMANCE OF THE CONVENTIONAL AND PROPOSED MACHINES UNDER DIFFERENT OPERATING CONDITIONS

Operating conditions	Light load		Normal load	
Machine types	Conv.	Prop.	Conv.	Prop.
Copper loss (W)	15.5		80	
RMS current (A)	2.9	2.8	6.55	6.4
Average torque (Nm)	5.07	7.02	9.68	13.71
Torque ripple (%)	4.14	3.53	5.85	3.92
Iron loss (W)	20.48	36.9	39.04	70
PM eddy-current loss (W)	8.96	7.1	8.43	12.9
Efficiency (%)	92.2	92.5	88.8	89.8
Power factor	0.76	0.77	0.43	0.45

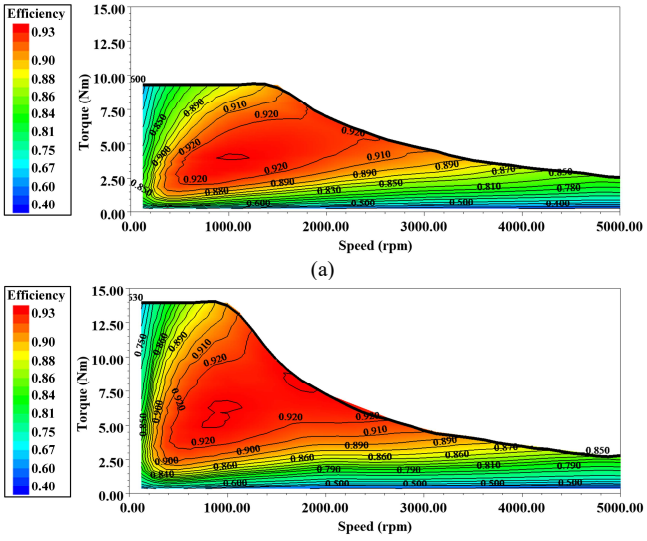

Fig. 21. Efficiency maps (I_{rms}=6.5 A, U_{dc}=340 V). (a) Conventional E-core FS machine. (b) Proposed DPM-FS machine.

D. Demagnetization Examination

In the proposed machine, the PM material adopts N35UH, and the demagnetization ability of the PMs is investigated under a two-times overload operation at 120 ℃. In this condition, the knee point coordinate of the N35UH is (-0.28 T, -980 kA/m). Fig. 22 illustrates the PM flux density distribution under two times of overload operation. As shown in Fig.22, the PMs are working in a flux density range from 0T to 1.6 T, which is greatly higher than the knee point of -0.28 T, indicating that PMs in the proposed machine are safe from demagnetization. Furthermore, multiple points are selected to analyze flux density variations in four PM segments with different magnetization directions and locations, as shown in Fig. 22. The flux densities of the selected points on 1st to 4th PMs are demonstrated in Fig. 23 (a) to (d). As shown in Fig. 23 (c), points C3 and D3 on the 3rd PM exhibit the minimum flux density. However, the flux densities are still larger than 0 T, validating that the PMs in the proposed machine have no risk of demagnetization.

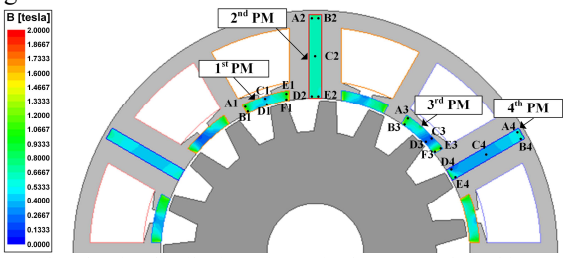

Fig. 22. Flux density distribution of PMs in the proposed machine under a two-times overload current.

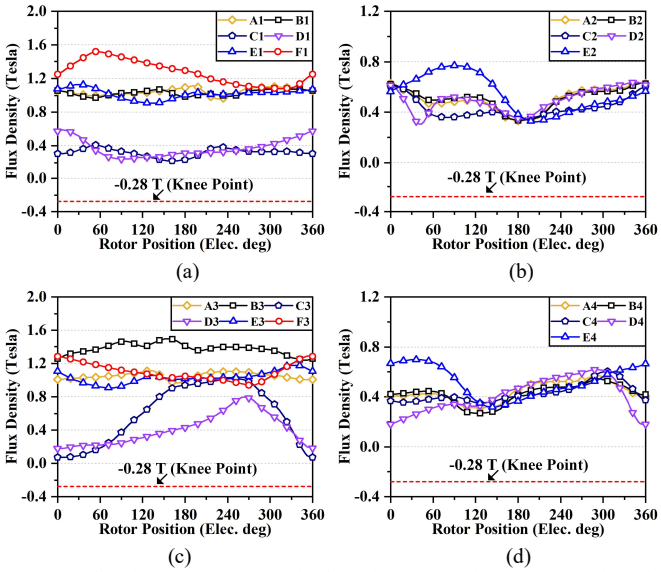

Fig. 23. Flux density variations of selected points on the PMs. (a) Selected points on 1st PM. (b) Selected points on 2nd PM. (c) Selected points on 3rd PM. (d) Selected points on 4th PM.

E. Comparative Study of Various Types of FS Machines

In this part, the proposed DPM-FS machine is further compared with four additional FSPM machines presented in published papers to demonstrate its merits. A C-core FS machine [20], a multi-tooth FS machine [19], a synergistic FS machine [27], and a U-shaped PM FS machine [24] are included in the comparison study, as shown in Fig. 24 (a) to (d), respectively. The stator outer diameter, air-gap length, stack length, PM volume, and copper loss have been kept the same among all machines to ensure a fair comparison. Meanwhile, the rotor pole pairs are selected as 19 in all machines except for

the U-shaped PM machine. Due to the consequent-pole stator PM design with different stator MMF pole pairs, 16 rotor poles are applied to utilize the same armature winding arrangement with other FS machines.

After performing a global optimization using NSGA-II, the open-circuit phase back EMF and on-load torque performance under the normal load condition of the conventional and the proposed machines are investigated. Table VIII lists the main design parameters and performance of these machines.

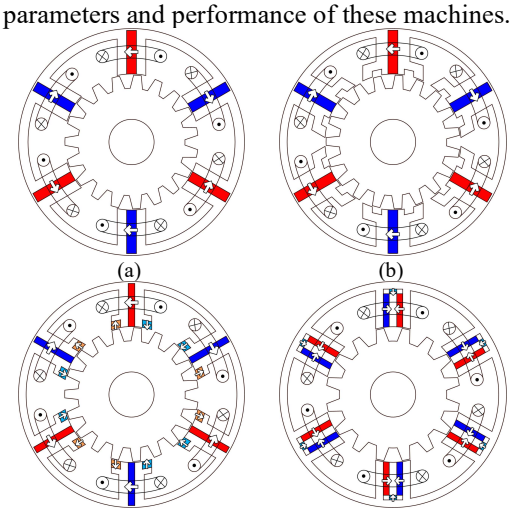

Fig. 24. Topologies of additional FS machines. (a) C-core FS machine [20]. (b) Multi-tooth FS machine [19]. (c) Synergistic FS machine [27]. (d) U-shaped PM FS machine [24].

TABLE VIII
DESIGN PARAMETERS AND PERFORMANCE OF THE FSPM MACHINES

	C-core FS	E-core FS	Multi-tooth FS	Synergistic FS	UPM FS	Prop. DPM-FS
N_s/N_r	6/19	12/19	6/19	6/19	6/16	12/19
L_{st} (mm)				50		
D_{so} (mm)*				120		
ω_r (r/min)				1000		
V_{PM} (mL)				36		
P_{copper} (W)				80		
E_{ph} (V)	86.4	90.5	118.7	103.4	105.3	129.2
I_{rms} (A)	6.64	6.54	6.02	6.69	5.58	6.40
T_{avg} (Nm)	10.3	9.7	11.8	12.5	10.5	13.7
T_{ripple} (%)	3.77	5.77	1.60	2.38	9.81	3.92
T_{avg}/V_{PM} (Nm/L)	285	269	328	346	292	381
η (%)*	89.5	88.8	87.2	89.7	89.1	89.8

* D_{so}, *and* η represent outer diameter and power efficiency, respectively.

Fig. 25 illustrates the open-circuit phase back EMF at an angular speed of 1000 r/min for the proposed DPM-FS machine and five conventional machines. The back EMF waveforms are shown in Fig. 25 (a), and the magnitudes of the fundamental harmonic are depicted in Fig. 25 (b). Due to the dual-set PM design of the proposed DPM-FS machine, the working harmonics of the air-gap flux density are effectively improved, resulting in the highest phase back EMF of 129.2 V among the six machines. The multi-tooth FS machine inserts extra stator teeth to improve the flux modulation effect, which also produces a high back EMF. In addition, the U-shaped PM FS machine eliminates the negative flux barrier effect on the end portion of stator PMs and enhances the flux-focusing effect due to the special PM arrangement. Consequently, the magnitude of back EMF is also prominent among the six machines. In contrast, the conventional C-core and E-core FSPM machines exhibit poor back EMFs.

Fig. 26 illustrates a comparison of the torque characteristics among conventional and proposed machines. As shown in Fig. 26 (a), the proposed DPM-FS machine exhibits the highest torque, while the C-core and E-core FS machines have poor torque performance among the six FSPM machines. This complies well with the results of open-circuit back-EMFs. However, multi-tooth and U-shaped PM FS machines have smaller slot areas, resulting in lower average torques than the synergistic FSPM machine. Moreover, the U-shaped PM FS machine exhibits significant torque ripple due to the even number of rotor poles. As shown in Fig. 26 (b), the average torque of the proposed DPM-FS machine exhibits the highest value at overload conditions, showing good overload performance. The multi-tooth FSPM machine exhibits a high average torque when the current is low, but it shows inferior torque values when the current increases due to severe magnetic saturation under a high electric load. The synergistic FS and U-shaped PM FS machines exhibit similar performance. In contrast, the performance of C-core and E-core FS machines is inferior. Furthermore, the proposed DPM-FS machine has the highest PM volumetric torque density and efficiency among the six machines, as shown in Table VIII. This demonstrates the cost-efficient and energy-efficient advantages of the proposed machine for potential industrial applications.

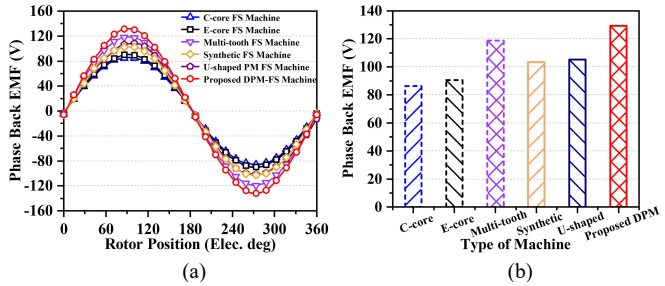

Fig. 25. Open-circuit phase back EMF of machines in comparison. (a) Waveforms. (b) Magnitudes of the fundamental harmonic.

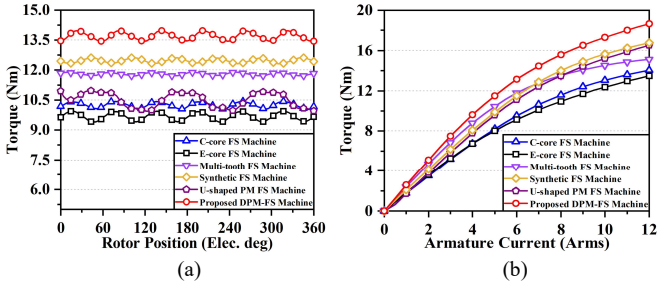

Fig. 26. Torque characteristics of machines in comparison. (a) Torque under the normal load condition. (b) Average torque vs. armature current.

VI. EXPERIMENTAL VERIFICATIONS

A prototype of the proposed machine is fabricated, and experiments are conducted to validate the theoretical analysis and FEA results. The main parts of the prototype are illustrated in Fig. 27. As shown in Fig. 27 (a) and (b), the stator core and rotor core are manufactured with laminated silicon steel sheets of B35A360. Fig. 27 (c) shows the stator assembly. The N35UH PM material is used to avoid demagnetization at high working temperatures. Additionally, the cogging torque and loading test rig are shown in Fig. 27 (d) and (e).

The open-circuit line back EMF is measured under a constant rated speed, which is shown in Fig. 28 (a). In this test, the prototype is driven by the load machine at 1000 r/min. Compared with the FEA-predicted result considering the stacking factor, the measured result shows good consistency, as shown in Fig. 28 (b) and (c). The error between the FEA-predicted and measured results is mainly due to the end-effect, stacking factor of stator and rotor cores, and manufacturing tolerance. Meanwhile, the total harmonic distortion (THD) of the measured line back EMF is slightly increased to 0.75% compared with 0.66% of the FEA-predicted result.

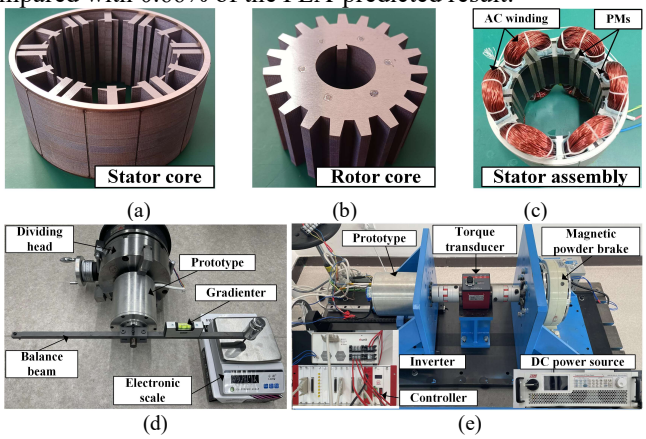

Fig. 27. Prototype main parts and the test rigs. (a) Stator core. (b) Rotor core. (c) Stator assembly. (d) Cogging torque test rig. (e) Loading test rig.

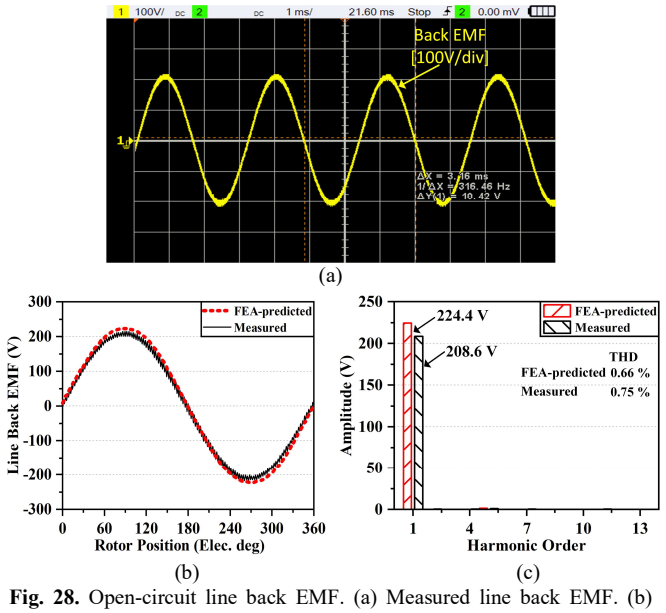

Fig. 28. Open-circuit line back EMF. (a) Measured line back EMF. (b) Comparison of line back EMF. (c) Harmonic distributions.

Fig. 29 shows the FEA-predicted and measured torque performance under light and normal load conditions. In the on-load test, a magnetic power brake is applied to generate the load, and a real-time digital controller with I_d=0 control strategy is used to control the prototype. In Fig. 29 (a) and (b), the phase currents are 2.8 A and 6.4 A, accordingly. In both load conditions, the measured torque shows an error of less than 10% compared to the FEA-predicted results. The difference between the measured and FEA-predicted results is mainly due to the end-effect, friction torque, and tolerances during the manufacturing process. In addition, the torque is measured at different values of armature currents, as shown in Fig. 30 (a). The measured results are in good agreement with the simulated results, exhibiting a low degree of error. Moreover, the cogging torque test is shown in Fig. 30 (b). The magnitude of the measured result is larger than the FEA simulation, mainly due to the manufacturing tolerances of the stator core, rotor poles, and PMs. Nevertheless, as shown in Table IX, the magnitude of the measured cogging torque is only 0.15 Nm, which has little influence on the stable operation of the machine.

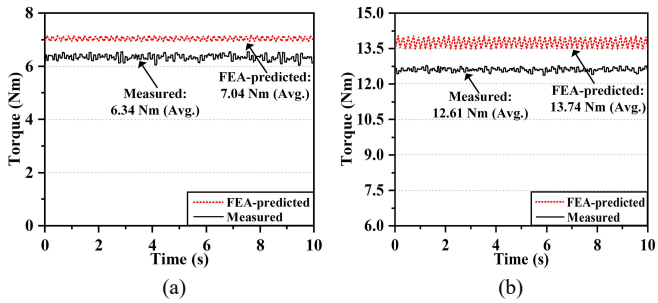

Fig. 29. FEA-predicted and measured torque under different load conditions. (a) Light load when phase current is 2.8A. (b) Normal load when phase current is 6.4A.

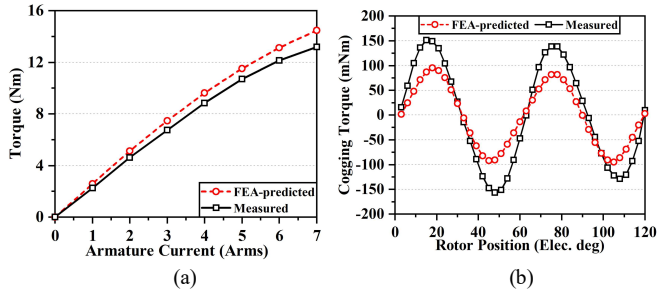

Fig. 30. FEA-predicted and measured torque characteristics. (a) Average torque vs. armature current. (b) Cogging torque.

TABLE IX
THE MEASURED AND FEA-PREDICTED RESULTS

	Measured	FEA-predicted
Open-circuit line back EMF (V)	208.6	224.4
Average torque under the light load condition (Nm)	6.34	7.04
Average torque under the normal load condition (Nm)	12.61	13.74
Cogging torque magnitude (Nm)	0.15	0.09

A vibration test has been conducted at a speed of 300 r/min to validate the proposed structural design. As shown in Fig.31, two acceleration sensors are attached to the housing of the prototype. The sensors detect acceleration signals, which are further processed by a dynamic signal analyzer to obtain the vibration spectrum.

Fig. 32 (a) and (b) shows the acceleration frequency response of sensor No.1 and No.2, respectively. f_r is defined as the rotation frequency. When the rotational speed is 300 r/min, f_r can be calculated as 5Hz. As shown in Fig. 32 (a) and (b), the frequencies of acceleration peaks detected by both sensors are related to the rotor pole numbers of $19kf_r$ (k=1,2,3,4…). Meanwhile, the maximum acceleration occurs at the frequency of 190 Hz ($38f_r$), and the magnitudes are 0.074 m/s^2 at position 1 and 0.054 m/s^2 at position 2, exhibiting a low vibration of the prototype. Moreover, a 3D FEA simulation of the stator assembly structure is conducted to investigate the natural

frequencies of the proposed machine. The values obtained reveal that the first-order natural frequency is as high as 5705.5 Hz, while the values for higher-order natural frequencies are even higher. The primary acceleration peaks of the machine occur at 95 Hz (19 f_r) and 190 Hz (38 f_r), which are far away from the natural frequencies. Therefore, there is no potential risk of resonance during the operation of the proposed machine.

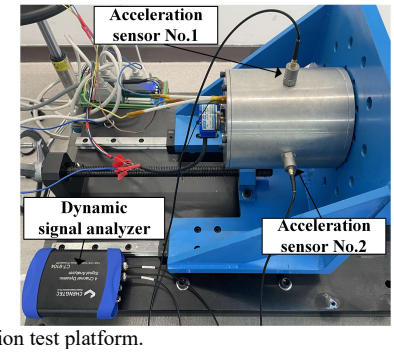

Fig. 31. Vibration test platform.

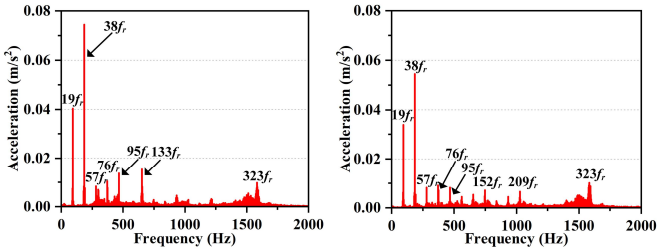

Fig. 32. Acceleration frequency response of the prototype. (a) Position 1. (b) Position 2.

VII. Conclusion

In this paper, a novel E-core DPM-FS machine is proposed. Compared with the conventional E-core FS machine, the proposed machine has an extra set of PMs inserted into the stator slot openings. Due to the artfully designed magnetization direction of slot PMs, the two PM sets have parallel main flux paths, which enhances the multi-working harmonics with positive contributions to total torque production and decreases the harmonics with negative contributions. Meanwhile, the magnetic saturation is notably decreased due to the addition of slot PMs. The open-circuit back EMF is increased by 42.8%, and the average torques under light and normal load conditions are elevated by 38.46% and 41.6%, respectively. Moreover, the proposed machine exhibits high efficiencies of over 90% across a wide range of loads and speeds. Finally, a prototype machine is fabricated, and the experiments show good consistency with the FEA results.

Acknowledgment

This work was supported by the National Natural Science Foundation of China under Project 52077187 and in part by the Research Grant Council of the Hong Kong Government under Project PolyU 152109/20E.

References

[1] Y. Chen, W. Fu, and X. Weng, "A concept of general flux-modulated electric machines based on a unified theory and its application to developing a novel doubly-fed dual-stator motor," *IEEE Trans. Ind. Electron.*, vol. 64, no. 12, pp. 9914–9923, Dec. 2017.

[2] K. T. Chau, C. C. Chan, and C. Liu, "Overview of permanent-magnet brushless drives for electric and hybrid electric vehicles," *IEEE Trans. Ind. Electron.*, vol. 55, no. 6, pp. 2246–2257, Jun. 2008.

[3] Z. Q. Zhu and Y. Liu, "Analysis of air-gap field modulation and magnetic gearing effect in fractional-slot concentrated-winding permanent-magnet synchronous machines," *IEEE Trans. Ind. Electron.*, vol. 65, no. 5, pp. 3688–3698, May 2018.

[4] Y. Shen, Q. Lu and Y. Li, "Design Criterion and Analysis of Hybrid-Excited Vernier Reluctance Linear Machine with Slot Halbach PM Arrays," *IEEE Trans. Ind. Electron.*, vol. 70, no. 5, pp. 5074–5084, May 2023.

[5] H. Hua, W. Hua, and G. Zhao, "General principle of symmetrical flux linkages in stator-permanent magnet machines," *IEEE Trans. Magn.*, vol. 57, no. 2, pp. 1–6, Feb. 2021.

[6] Y. Gao, T. Kosaka, Y. Liu, M. Doppelbauer, and R. Qu, "Comparative Analysis of Double Flux Modulation Permanent Magnet Machines With Different Stator PM Arrangements," *IEEE Trans. on Ind. Appl.*, vol. 58, no. 2, pp. 1941–1951, Mar. 2022.

[7] M. Cheng, P. Han, and W. Hua, "General airgap field modulation theory for electrical machines," *IEEE Trans. Ind. Electron.*, vol. 64, no. 8, pp. 6063–6074, Aug. 2017.

[8] D. Li, R. Qu, and J. Li, "Topologies and analysis of flux-modulation machines," in *2015 IEEE Energy Conversion Congress and Exposition (ECCE)*, Montreal, QC, Canada, Sep. 2015, pp. 2153–2160.

[9] Y. Gao, D. Li, R. Qu, and J. Li, "Design procedure of flux reversal permanent magnet machines," *IEEE Trans. on Ind. Appl.*, vol. 53, no. 5, pp. 4232–4241, Sep. 2017.

[10] H. Yang, H. Lin, Z. Q. Zhu, S. Lyu, and Y. Liu, "Design and analysis of novel asymmetric-stator-pole flux reversal PM machine," *IEEE Trans. Ind. Electron.*, vol. 67, no. 1, pp. 101–114, Jan. 2020.

[11] H. Yang, Z. Q. Zhu, H. Lin, H. Li, and S. Lyu, "Analysis of consequent-pole flux reversal permanent magnet machine with biased flux modulation theory," *IEEE Trans. Ind. Electron.*, vol. 67, no. 3, pp. 2107–2121, Mar. 2020.

[12] X. Zhao, S. Niu, and W. Fu, "A novel Vernier reluctance machine excited by slot PMs and zero-sequence current for electric vehicle," *IEEE Trans. Magn.*, vol. 55, no. 6, pp. 1–5, Jun. 2019.

[13] Y. Shen, Z. Zeng, Q. Lu, and Y. Li, "Investigation of a modular linear doubly salient machine with dual-PM in primary yoke and slot openings," *IEEE Trans. Magn.*, vol. 55, no. 6, pp. 1–6, Jun. 2019.

[14] G. Ming, L. Wu, L. Zhang, and J. Zhu, "Comparative study of novel doubly fed doubly salient PM machines with different stator/rotor-pole number combinations," *IEEE Trans. Magn.*, vol. 57, no. 6, pp. 1–5, Jun. 2021.

[15] D. Li, R. Qu, J. Li, W. Xu, and L. Wu, "Synthesis of flux switching permanent magnet machines," *IEEE Trans. Energy Convers.*, vol. 31, no. 1, pp. 106–117, Mar. 2016.

[16] Y. Shen, Q. Lu, H. Li, J. Cai, X. Huang, and Y. Fang, "Analysis of a Novel Double-Sided Yokeless Multitooth Linear Switched-Flux PM Motor," *IEEE Trans. Ind. Electron.*, vol. 65, no. 2, pp. 1837-1845, Feb. 2018.

[17] Y. Shi, L. Jian, J. Wei, Z. Shao, W. Li, and C. C. Chan, "A new perspective on the operating principle of flux-switching permanent-magnet machines," *IEEE Trans. Ind. Electron.*, vol. 63, no. 3, pp. 1425–1437, Mar. 2016.

[18] W. Hua, H. Zhang, M. Cheng, J. Meng, and C. Hou, "An outer-rotor flux-switching permanent-magnet-machine with wedge-shaped magnets for in-wheel light traction," *IEEE Trans. Ind. Electron.*, vol. 64, no. 1, pp. 69–80, Jan. 2017.

[19] J. T. Chen, Z. Q. Zhu, and D. Howe, "Stator and Rotor Pole Combinations for Multi-Tooth Flux-Switching Permanent-Magnet Brushless AC Machines," *IEEE Trans. Magn.*, vol. 44, no. 12, pp. 4659–4667, Dec. 2008.

[20] J. T. Chen, Z. Q. Zhu, S. Iwasaki, and R. P. Deodhar, "Influence of slot opening on optimal stator and rotor pole combination and electromagnetic performance of switched-flux PM brushless AC machines," *IEEE Trans. on Ind. Appl.*, vol. 47, no. 4, pp. 1681–1691, Jul. 2011.

[21] J. T. Chen, Z. Q. Zhu, S. Iwasaki, and R. P. Deodhar, "A novel E-core switched-flux PM brushless AC machine," *IEEE Trans. on Ind. Appl.*, vol. 47, no. 3, pp. 1273–1282, May 2011.

[22] Z. Liang, Y. Gao, D. Li, and R. Qu, "Investigate of a flux switching permanent magnet machine with alternative flux bridges," in *2019 IEEE Energy Conversion Congress and Exposition (ECCE)*, Baltimore, MD, USA, Sep. 2019, pp. 6548–6554.

[23] Y. Gao, D. Li, R. Qu, H. Fang, H. Ding, and L. Jing, "Analysis of a novel consequent-pole flux switching permanent magnet machine with flux

bridges in stator core," *IEEE Trans. Energy Convers.*, vol. 33, no. 4, pp. 2153–2162, Dec. 2018.

[24] H. Yang, Y. Li, H. Lin, Z. Q. Zhu, and S. Lyu, "Principle Investigation and Performance Comparison of Consequent-Pole Switched Flux PM Machines," *IEEE Trans. Transport. Electrific.*, vol. 7, no. 2, pp. 766–778, Jun. 2021.

[25] D. Kim, H. Hwang, S. Bae, and C. Lee, "Analysis and Design of a Double-Stator Flux-Switching Permanent Magnet Machine Using Ferrite Magnet in Hybrid Electric Vehicles," *IEEE Trans. Magn*., vol. 52, no. 7, pp. 1–4, Jul. 2016.

[26] Z. Xiang, L. Quan, and X. Zhu, "A New Partitioned-Rotor Flux-Switching Permanent Magnet Motor With High Torque Density and Improved Magnet Utilization," *IEEE Trans. Appl. Supercond.*, vol. 26, no. 4, pp. 1–5, Jun. 2016.

[27] S. Cai, H. Chen, X. Yuan, Y.-C. Wang, J.-X. Shen, and C. H. T. Lee, "Analysis of Synergistic Stator Permanent Magnet Machine With the Synergies of Flux-Switching and Flux-Reversal Effects," *IEEE Trans. Ind. Electron.*, vol. 69, no. 12, pp. 12237–12248, Dec. 2022.

[28] C. Chen, X. Ren, D. Li, R. Qu, K. Liu, and T. Zou, "Torque performance enhancement of flux-switching permanent magnet machines with dual sets of magnet arrangements," *IEEE Trans. Transport. Electrific.*, vol. 7, no. 4, pp. 2623–2634, Dec. 2021.

[29] J. Huang, W. Fu, S. Niu, and X. Zhao, "Comparative analysis of different permanent magnet arrangements in a novel flux modulated electric machine," *IEEE Access*, vol. 9, pp. 14437–14445, 2021.

[30] Y. Li, H. Yang, H. Lin, W. Liu, and X. Zhao, "Torque Generation Mechanism and Performance Evaluation of a Dual-Sided PM Machine With Stator U-Shaped Magnets," *IEEE Trans. on Ind. Appl.*, vol. 58, no. 1, pp. 250–260, Jan. 2022.

[31] X. Zhao and S. Niu, "Design and optimization of a new magnetic-geared pole-changing hybrid excitation machine," *IEEE Trans. Ind. Electron.*, vol. 64, no. 12, pp. 9943–9952, Dec. 2017.